The Astrophysical Journal, 586:579–591, 2003 March 20

THE LONG-TERM EVOLUTION OF AR 7978: THE SCALINGS OF THE CORONAL PLASMA PARAMETERS WITH THE MEAN PHOTOSPHERIC MAGNETIC FIELD

L. van Driel-Gesztelyi,[1,2,3,4] P. Démoulin,[2] C. H. Mandrini,[5,6] L. Harra,[3] and J. A. Klimchuk[7]

Received 2002 March 14; accepted 2002 November 27

ABSTRACT

We analyze the evolution of the fluxes observed in X-rays and correlate them with the magnetic flux density in active region (AR) NOAA 7978 from its birth throughout its decay, for five solar rotations. We use *Solar and Heliospheric Observatory* Michelson Doppler Imager (MDI) data, together with *Yohkoh* Soft X-Ray Telescope (SXT) and *Yohkoh* Bragg Crystal Spectrometer (BCS) data, to determine the global evolution of the temperature and the emission measure of the coronal plasma at times when no significant brightenings were observed. We show that the mean X-ray flux and derived parameters, temperature and emission measure (together with other quantities deduced from them, such as the density and the pressure), of the plasma in the AR follow power-law relationships with the mean magnetic flux density ($\bar{B}$). The exponents (b) of these power-law functions ($a\bar{B}^b$) are derived using two different statistical methods, a classical least-squares method in log-log plots and a nonparametric method, which takes into account the fact that errors in the data may not be normally distributed. Both methods give similar exponents, within error bars, for the mean temperature and for both instruments (SXT and BCS); in particular, b stays in the range [0.27, 0.31] and [0.24, 0.57] for full-resolution SXT images and BCS data, respectively. For the emission measure, the exponent b lies in the range [0.85, 1.35] and [0.45, 1.96] for SXT and BCS, respectively. The determination of such power-law relations, when combined with the results from coronal heating models, can provide us with powerful tools for determining the mechanism responsible for the existence of the high-temperature corona.

Subject headings: Sun: corona — Sun: magnetic fields — Sun: X-rays, gamma rays

1. INTRODUCTION

The solar corona, at a temperature of above 10^6 K, originates from a constant energy supply to the atmosphere. This energy input increases both the temperature and the density of the plasma by orders of magnitude. Most of the present coronal heating models propose that this energy has a magnetic origin; however, no consensus has yet been reached about the physical mechanism by which the magnetic energy is converted into heat. To solve this problem is difficult, since it is not possible to measure the heating flux directly; in fact, only averaged and indirect physical parameters can be determined (such as the UV and X-ray fluxes and the density and temperature of the plasma). To make further progress, it is important to establish how these physical quantities, whose variations are the consequence of the energy input, relate to the magnetic field. By combining these results with the relevant models, one can attempt to determine the mechanism responsible for the heating of the corona.

The development of high-resolution X-ray and extreme-UV (EUV) imaging techniques (Vaiana et al. 1977; Underwood & McKenzie 1977; Golub & Herant 1989; Tsuneta et al. 1991; Delaboudinière et al. 1995; Handy et al. 1999) has enabled extensive studies of the density and temperature structure of the solar corona. Temperature and emission measure (EM) information can be obtained from ratios of images taken with two different broadband X-ray or narrowband EUV filters (Vaiana, Krieger, & Timothy 1973; Gerassimenko & Nolte 1978; Hara et al. 1992; Hara 1996). The different approaches taken include mean temperature and EM diagnostics of active and quiet coronal regions (Vaiana et al. 1973; Hara et al. 1992; Brosius et al. 1997). The obtained parameter values depend on the temperature sensitivity range of the instruments and reflect the multitemperature (1–5 MK) nature of the coronal plasmas. In all cases, however, there is a significant difference in temperature and EM (density) between active and quiet regions: e.g., for the *Yohkoh* Soft X-ray Telescope (SXT) a factor of 2 in temperature [$(2.7–5.7) \times 10^6$ K] and 2 orders of magnitude in EM (1×10^{26} to 5×10^{28} cm^{-5}; e.g., Hara et al. 1992). Spatially unresolved high (4×10^6 K) and low (2.5×10^6 K) activity level temperatures and differential EMs were determined from full-Sun X-ray spectra observed with the *Yohkoh* Bragg Crystal Spectrometer (BCS; Watanabe et al. 1995). Other studies concentrated on obtaining plasma parameters of individual X-ray and EUV loops (e.g., Arndt, Habbal, & Karovska 1994; Kano & Tsuneta 1995, 1996; Yoshida et al. 1995; Porter & Klimchuk 1995; Aschwanden et al. 2000).

Several authors (Rosner, Tucker, & Vaiana 1978; Serio et al. 1981; Golub et al. 1980; Porter & Klimchuk 1995; Kano & Tsuneta 1995; Aschwanden et al. 2000; Yashiro & Shibata 2001) have determined how coronal plasma parameters (temperature or pressure) depend on the loop length or magnetic field strength in active regions (ARs). The aim has generally been to combine the observations with theoretical

[1] Centre for Plasma Astrophysics, Katholieke Universiteit Leuven, Celestijnenlaan 200B, 3001 Leuven, Belgium; lidia.vandriel@obspm.fr.
[2] Observatoire de Paris, LESIA, FRE 2461 (CNRS), F-92195 Meudon Principal Cedex, France; pascal.demoulin@obspm.fr.
[3] Mullard Space Science Laboratory, Holmbury St. Mary, Dorking, Surrey RH5 6NT, UK; lkh@mssl.ucl.ac.uk.
[4] Konkoly Observatory, P.O. Box 67, H-1525 Budapest, Hungary.
[5] Member of the Carrera del Investigador Científico, CONICET, Argentina.
[6] Instituto de Astronomía y Física del Espacio, IAFE, Casilla de Correos 67, Sucursal 28, 1428 Buenos Aires, Argentina; mandrini@iafe.uba.ar.
[7] Naval Research Laboratory, Code 7675, Washington, DC 20375-5352; klimchuk@nrl.navy.mil.

scaling laws from quasi-steady loop models to test the validity of these models or derive scaling laws for the heating rate and thereby constrain coronal heating theories.

Using *Skylab* soft X-ray images of ARs and X-ray bright points, together with longitudinal magnetograms, Golub et al. (1980) determined that the average pressure was related to the average magnetic field through a power-law function with an exponent in the range [1.5, 1.9]. Yashiro & Shibata (2001) reexamined the data and concluded that they are better represented by an exponent of 1.11 ± 0.64. They also analyzed the magnetic properties of 31 different ARs observed by *Yohkoh* and found that the pressure scales with the mean magnetic field with a power of 0.78 ± 0.23. In this same work, Yashiro & Shibata (2001) computed average quantities for a larger set of 64 ARs and found that the temperature scales with AR size with an exponent of 0.28 ± 0.08, while the exponent linking the pressure to the AR size is -0.16 ± 0.21.

Other studies have considered individual loops, rather than entire ARs or bright points. Porter & Klimchuk (1995) found that temperature and loop length are uncorrelated and that the pressure varies inversely with length to approximately the first power for a set of 47 *Yohkoh* loops identified in different ARs. The density of these loops also varies inversely with length to the first power (Mandrini, Démoulin, & Klimchuk 2000a). Kano & Tsuneta (1995) examined 32 *Yohkoh* loops belonging to the same AR and found that the temperature scales with length to a power of 0.36, which is consistent with the Porter & Klimchuk (1995) result. No explicit exponent value was given for the density. Aschwanden et al. (2000) studied cooler loops observed in a single AR by the *Solar and Heliospheric Observatory* (*SOHO*) EUV Imaging Telescope and obtained pressure-length exponents in the range $[-0.96, -0.31]$, depending on which pair of filters was used. They also obtained pressure–field strength exponents in the range [0.06, 0.20], although it is very difficult to identify the magnetic footpoints of individual loops. In this paper, we follow a different approach as discussed below.

To determine useful relationships between the plasma physical parameters and the magnetic field, we need to consider their largest possible range of variation. Previous studies (see above) were mostly based on observations of young ARs or individual loops; therefore, the range of the magnetic field strengths considered is relatively narrow. Studying the long-term evolution (from the emergence through the decay phase) of an AR, we have the chance to consider a wider interval of magnetic field strengths and plasma conditions. Furthermore, instead of following the detailed evolution of loops, we can analyze the global evolution of the AR coronal plasma. This reduces the statistical noise, in particular during the late phase of the AR evolution when individual loops are difficult to observe.

A perfect target AR for such analysis appeared during the minimum between cycles 22 and 23, from 1996 July to December, and it was well observed with instruments on board *SOHO* and *Yohkoh* (in particular, the Michelson Doppler Imager [MDI], SXT, and BCS). This region was identified as AR 7978 (NOAA number) when it first appeared on 1996 July 4 in the southern hemisphere. It was the only sizable and long-lived AR on the solar disk during five solar rotations, so the BCS (full disk) instrument could be used even in the AR decaying phase. Its global evolution was analyzed in the context of the present knowledge of the long-term evolution of ARs (van Driel-Gesztelyi 1998). AR 7978 had a simple bipolar magnetic configuration, which was maintained throughout its lifetime. Its magnetic field strength steadily decreased because of diffusion during the successive solar rotations. Since the AR was isolated, it evolved almost undisturbed, without being subjected to major cancellation events that could have led to its premature disappearance. For these reasons, we can explore the effect of magnetic field strength on the magnitude of the coronal emission and on the plasma parameters considering nearly the largest possible range of variations.

The aim of our work is to derive the long-term evolution of the coronal physical parameters and to correlate the global plasma conditions with the mean magnetic field. First, we summarize the relevant characteristics of the instruments used in § 2. Then, in § 3 we describe the temporal evolution of the magnetic field and of the mean coronal X-ray flux (SXT). We also explain the methodology used throughout the paper (selection of the quiet periods, analysis of the statistical errors, and probable systematic biases). In §§ 4 and 5 we describe the evolution of the temperature and the EM (SXT and BCS), respectively. We show that all these quantities have a power-law dependence on the mean magnetic flux density ($\bar{B}$). We derive the power law of the mean plasma density and pressure with $\bar{B}$ in §§ 6 and 7, and we summarize the results and conclude in § 8.

2. THE DATA

2.1. *SOHO*/*MDI*

The Michelson Doppler Imager is one of 12 experiments on board the *SOHO* spacecraft, which was launched on 1995 December 2. The Solar Oscillation Investigation (SOI) uses the MDI instrument to probe the interior of the Sun by measuring the photospheric manifestation of solar oscillations (Scherrer et al. 1995). The instrument images the Sun on a 1024×1024 CCD camera through a series of increasingly narrow filters. The final elements, a pair of tunable Michelson interferometers, enable MDI to record filtergrams with a FWHM bandwidth of 100 mÅ. Several times each day, polarizers are inserted to determine the line-of-sight magnetic field. In this paper, we analyze 5 minute–averaged magnetograms of the full disk with a 96 minute cadence and a pixel size of $2''$.

The noise in the magnetograms originates from two main components: photon shot noise and leakage from the Doppler signal. Single magnetograms are limited by the shot noise to about ± 10 G and 5 minute–averaged maps, such as the ones used here, to about ± 3 G. This is because over a 5 minute interval most *P*-modes execute almost one complete cycle, so the *P*-mode leakage is smaller. There is some noise of about the 2–3 G level from granulation as well. The shutter noise introduces a 0.5 G uncertainty. Assuming that the low-level signal is purely noise, Liu & Norton (2001)[8] found a 9 G level for the 5 minute magnetograms used in this paper, which is an upper bound for the noise.

Liu & Norton (2001) analyzed MDI measurement errors and found that MDI underestimates velocity and magnetic field up to 5% and 15%, respectively, using circular and linear polarizations. The level of underestimation depends on

[8] See http://soi.stanford.edu/data/cal/mag_data.html#nonlinearity.

both the field strength and disk position. The strong-field regions are the most affected ($\geq$2000 G). Another problem with MDI magnetic field measurements is that in very dark umbrae with a strong field, when the combined spacecraft and solar rotational velocities are greater than 2 km s^{-1}, the MDI algorithm breaks down and the magnetic field strength drastically decreases to values of several hundred Gauss, instead of the kilogauss level expected. The presence of such corrupted pixels affects magnetic flux measurements.

2.2. *Yohkoh*/*SXT*

The Soft X-Ray Telescope (Tsuneta et al. 1991) provided full-disk (4.″92 pixel^{-1}, referred to as half resolution below) and partial-frame (2.″46 pixel^{-1}, referred to as full resolution below) images during the studied interval taken alternately with the thin Al 0.1 μm and Dagwood AlMgMn filters. The sensitivity of the filters provides observations in a logarithmic temperature range between 6 and 7. To compute the temperature T and the EM as a function of time, we use both the partial- and full-resolution images taken with the above two filters, integrating the soft X-ray emission over the entire region and calculating the filter ratios averaging over two total *Yohkoh* orbits. However, since the data number (DN) count is not conserved in saturated pixels in the half-resolution images, we only use the full-resolution data for the present analysis. Since the counts in the integrated fluxes are large, uncertainties in the T and EM determinations are dominated by photometric calibration errors rather than counting statistics. These systematic uncertainties are roughly 0.1 in log T and 0.2 in log EM (Klimchuk & Gary 1995; Hara et al. 1992).

It is noteworthy that the filter pair used by us (Al.1/AlMgMn) was recently shown to be the most reliable of all of the SXT filter pairs used for temperature analysis. Shimojo, Hara, & Kano (2002) calculated the temperature responses of the SXT analysis filters using the CHIANTI (Version 3) package released by Dere et al. (2001) and compared the resulting temperatures with the ones computed with the Mewe databases, which is the standard database for *Yohkoh*/SXT. They obtained good correspondence between the temperatures calculated with the Mewe and CHIANTI database for the Al.1/AlMgMn filters, with 30%–40% difference between the two at 4–5 MK for the Al.1/Al12 filter pair.

The sizes of the partial-frame full-resolution (2.″46 pixel^{-1}) images were set to follow the increasing area of the AR: 128 $\times$ 128 pixel^2 during the first (July 4–10) and second (central meridian passage [CMP] on August 2) rotations, 192 $\times$ 192 pixel^2 during the third rotation (CMP on August 30), 320 $\times$ 256 pixel^2 during the fourth rotation (CMP on September 26), and 192 $\times$ 192 pixel^2 during the fifth rotation (CMP on October 23). The exposure times used gradually increased, from 28–1355 ms during the first rotation up to 7582 ms during the fourth and fifth rotations. These special adjustments were done because AR 7978 was the only sizable AR on the Sun and received special attention from *Yohkoh* chief observers.

2.3. *Yohkoh*/*BCS*

The Bragg Crystal Spectrometer on board *Yohkoh* (Culhane et al. 1991) consists of four spectrometers with wavelength ranges encompassing the resonance lines of helium-like sulfur (5.04 Å), calcium (3.18 Å), and iron (1.85 Å), along with hydrogen-like iron (1.78 Å). It is a full-Sun instrument with a temporal resolution of 3 s in flare mode, although for the nonflare emissivities of this study, we use integration times in the range 3–1200 s. BCS provides data with a sensitivity $\approx$10 times larger than previous similar experiments. In particular, the S XV channel has a sensitivity $\approx$60 times larger, giving us the opportunity to study low-emissivity cases, as is the long-term evolution of AR 7978. Using BCS we have been able to analyze the AR at its CMP during four rotations. After the fourth passage, the emission from the region became too weak to derive accurate plasma parameters.

3. OBSERVATIONS

3.1. *Evolution of the Magnetic Field*

Flux emergence started at S10, E31 on 1996 July 4 in a dominantly negative polarity environment, west of an old and dispersed bipolar region. By 1996 July 6, the first well-formed sunspots of NOAA 7978 were observed, and the fast growth of the magnetic flux lasted until at least July 10 (van Driel-Gesztelyi et al. 1999b). There was a second episode of flux emergence in the AR, which started while the AR was on the invisible side of the Sun and continued for a few days after the AR rotated onto the disk for the second time. The magnetic field of the AR was clearly distinguishable from the so-called background field for at least seven solar rotations (we limit our analysis to the first five rotations during which full-resolution SXT data of the AR are available). We identify the region as AR 7978 along all the rotations, although in fact it was denoted as NOAA 7981 and NOAA 7986 in the second and the third rotations, respectively (Fig. 1). After the spots disappeared (from the fourth rotation on), the region did not have a NOAA number any longer, but we still refer to it as AR 7978.

Using *SOHO*/MDI magnetograms, we measured the total unsigned magnetic flux of the AR during the emergence and four more consecutive CMPs. We drew the magnetic boundary of the AR "by hand," relying on the detection by the human eye of a steep magnetic field gradient at that location, on magnetic maps displayed in the same dynamic range (Fig. 1). Such a method brings in subjective errors, but after carrying out several series of measurements, we did not find a dispersion larger than about 10% for the magnetic area and flux. The peak flux was reached during the third rotation (2.4×10^{22} Mx; see Fig. 2); this was due to an increase of the negative flux creating a roughly 10% flux imbalance in the AR. The imbalance was due to the fact that the AR emerged in a dominantly negative polarity magnetic environment, and as its flux diffused and its magnetic area grew, more and more of this preexisting negative flux was included in the measurements. Another effect of a dominantly negative polarity magnetic environment is that the positive flux of the dispersing AR has a better chance to cancel than the negative-polarity counterpart. Later on, the total flux decreased slowly and even increased during the last three rotations (October to December) because of an increasing level of small-scale new flux emergence and the ever-increasing area (van Driel-Gesztelyi et al. 1999b).

Because of magnetic dispersal, the magnetic area of the AR increased roughly linearly at a rate of 1.28×10^4 km^2

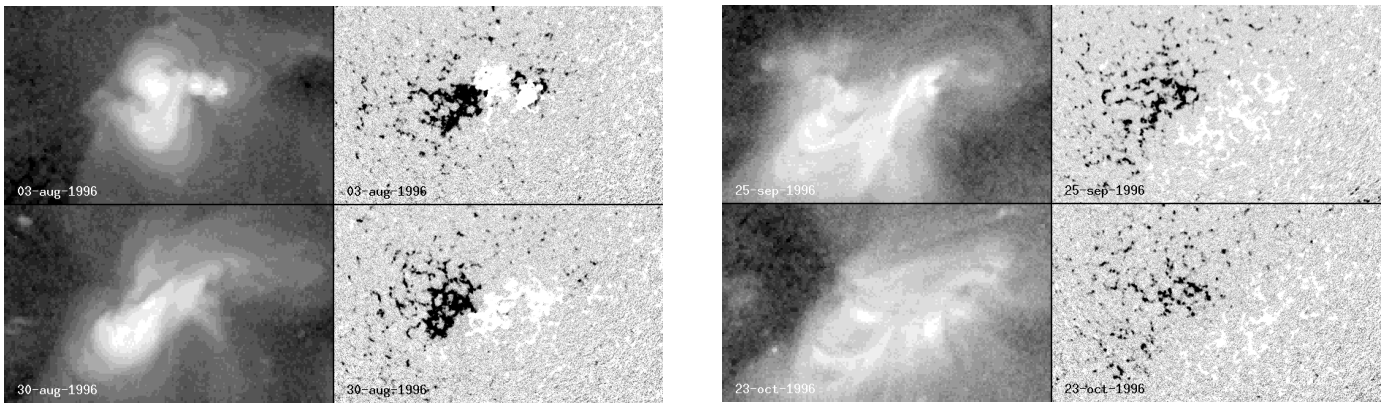

FIG. 1.—Long-term evolution of the soft X-ray emission (*Yohkoh* /SXT) and photospheric longitudinal magnetic field (*SOHO*/MDI) for AR 7978. This AR started emerging on 1996 July 4. The evolution from the second to the fifth rotations is shown here at CMPs. The AR is basically bipolar with sheared coronal loops joining opposite polarities (black and white gray levels on the MDI magnetograms). The brightness of the coronal loops is decreasing as the AR decays.

s^{-1} (Fig. 2). The magnetic flux density $\bar{B}$ (defined as the total magnetic flux divided by the AR surface area), which is a measure of the mean magnetic field, reached the highest level (188 Mx cm^{-2}) by the fourth day of the first flux emergence episode and steadily decreased after that in spite of the second episode of flux emergence (Fig. 3). Note that when deriving the magnetic flux density, we included both the strong umbral field and the pixels with low magnetic field value, because we were interested in deriving how the *global* evolution of the magnetic field in an AR is related to the evolution of the *global* plasma parameters.

The recently discovered MDI measurement errors (Liu & Norton 2001) described in § 2.1 must affect our magnetic flux density values. The magnetic flux density is found to be a factor f underestimated ($f \approx [0.7,\ 0.9]$, which depends on both the field strength and the velocity). Another indication of the underestimation in MDI measurements comes from the results of Berger & Lites (2002), who made a detailed comparison of the MDI and ASP (Advances Stokes Polarimeter) responses. They found that the MDI response saturates when the flux density is above ≈1200 G. For all rotations of AR 7978, at the times of our data points, the measured field stays below that value, so that we are in the linear regime of the magnetograph in which MDI underestimates the flux density by a factor of ≈0.64 compared to ASP. It is worth noting that any factor that is independent of B would not affect the exponents in our power laws, derived below, and thus would have no effect on the conclusions. Another known MDI error is the appearance of corrupted pixels in dark umbrae. We made $B-I_c$ plots for the data used on July 10, when the darkest umbrae were present in our data set, but found no trace of corrupted pixels.

3.2. *Selection of the Quiet Periods Using GOES and SXT*

The *Geostationary Operational Environmental Satellites* (*GOES*) provide soft X-ray irradiance measurements in the 1–8 and 0.5–4 Å ranges. Since with this analysis we intend to test coronal heating models, we have used the temporal evolution of fluxes measured in the *GOES* 9 softer channel, as well as with SXT, to select SXT and BCS data outside flaring periods. That is to say, periods with flares above *GOES* class B or with a small SXT flux enhancement (above 10% of the AR flux and lasting a few minutes or more) are removed from the data set. However, since microflares occur at all levels, it is difficult to define a threshold below which we could be confident that our data represent the nonflaring state of the AR.

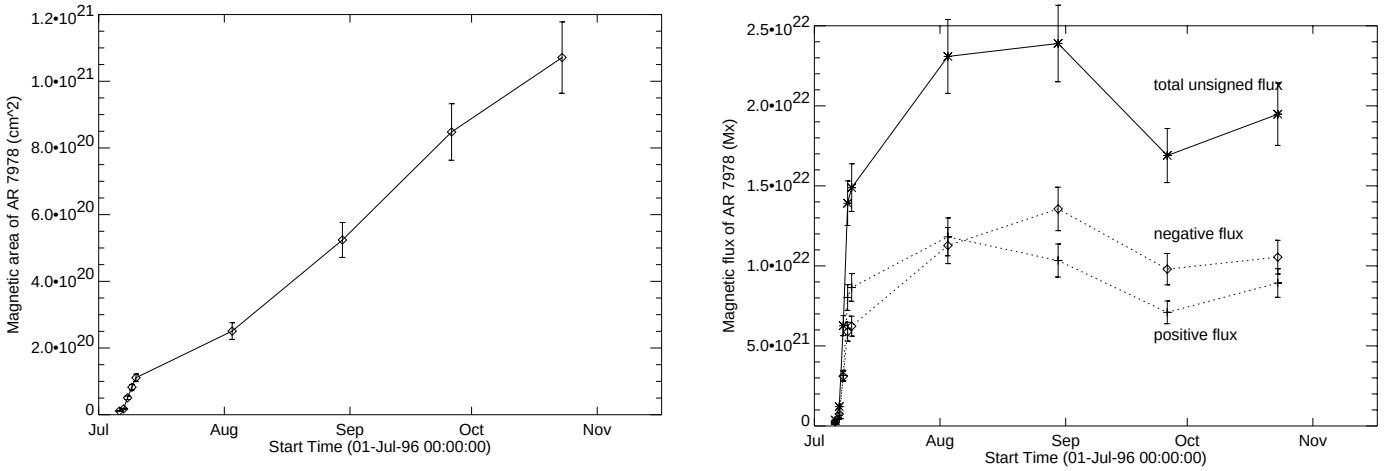

FIG. 2.—Evolution of the total AR area and of the magnetic flux vs. time. Longitudinal MDI magnetograms at CMPs are used.

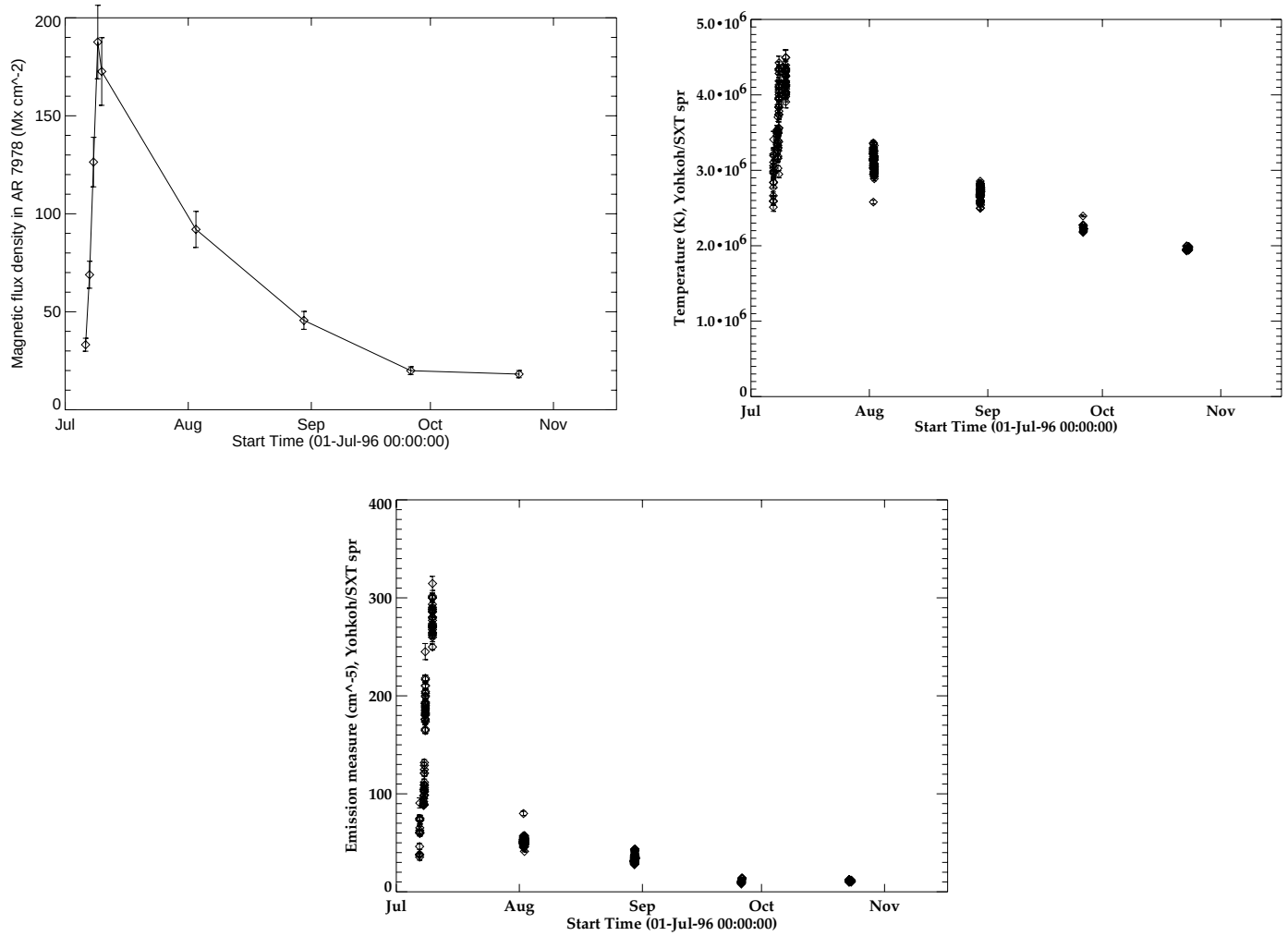

FIG. 3.—Evolution of the mean magnetic flux density $\bar{B}$ (AR flux divided by its area as shown in Fig. 2), the mean SXT temperature, and the mean SXT EM vs. time.

GOES data can be used to determine temperature and EM. However, *GOES* fluxes appeared to be contaminated by bremsstrahlung of energetic particles in the outer radiation belts of the Earth. This contamination was significant from August 20 until the end of October, dominating the flux in the harder channel (Orlando et al. 2000). For example, a steady oscillation with a period of 1 day was observed during September (see Fig. 3*a* of Sterling 1999). Since each *GOES* is a geostationary satellite, this was interpreted as the recurrent effect of the particle belts in the Earth's magnetosphere. That is why we have decided not to use filter ratios to derive temperature and EM from *GOES* data. It is noteworthy that the soft X-ray irradiance, outside flaring times, increased steeply during flux emergence and decreased during the decay phase (van Driel-Gesztelyi et al. 1999b).

3.3. *Statistics Used to Derive the Power Laws*

As shown below, we find that the mean X-ray flux, temperature, and EM have power-law relationships with the mean magnetic field ($\bar{B}$). The slope of the power law is first derived by a classical least-squares method in log-log plots. This assumes that the errors in the data are normally distributed (i.e., have a Gaussian distribution). However, since the real errors are unlikely to be normally distributed (at least for SXT; see the detailed study of Porter & Klimchuk 1995), we also use a nonparametric statistical method. This second method considers the rank ordering of the data rather than the data values, so it does not depend on the form of the error distribution. Because the results of a classical least-squares fit can be distorted by a few points that are far from the fitted curve (outliers), and because the formal uncertainty of the fit σ (the rms deviation of the data from the fit) is usually an underestimate of the true error, we quote an error range of $\pm 3\ \sigma$ (corresponding to a 99% confidence interval). For the nonparametric method, which is less influenced by outlier points, we quote a 90% confidence interval (see Porter & Klimchuk 1995 for further details). We keep this interval except for the BCS data, where the upper end of the interval is not well defined because of the relatively small number of data points. For these cases, the maximum values represent confidence levels of 59% and 82% for the BCS temperature and EM, respectively.

3.4. *Evolution of the SXT Fluxes*

We have measured the total flux emitted in soft X-rays by AR 7978 and have divided it by the area from which the emission came to get a mean flux density. The fluxes, as well as the temperature and EM (see below), were measured

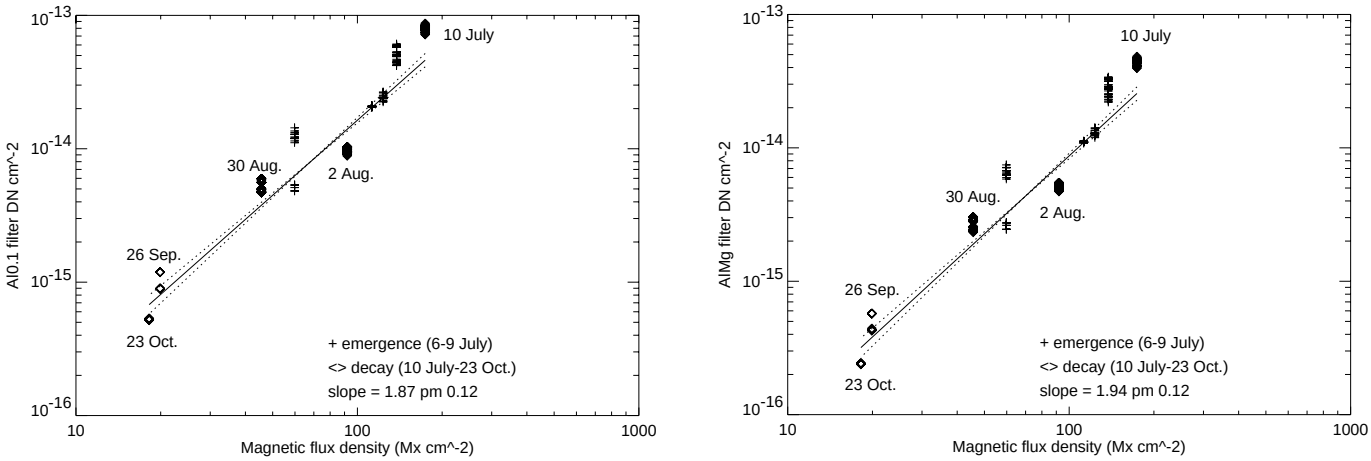

FIG. 4.—Plot of log-log curve of the fluxes per unit surface area observed with the Al.1 and AlMgMn filters of SXT (full resolution) vs. magnetic flux density ($\bar{B}$). The solid line shows the linear least-squares fit, and the two dotted lines correspond to the 3 σ error in the slope of the solid curve. Only the decaying phase (*diamonds*) is included in the least-squares fit.

during two full spacecraft orbits around each CMP of the AR between August and October, while during July measurements were done daily. During this latter period the data used covered 70 minutes on average, representing 26 filter ratios, while during the decay phase we analyzed data extending over a mean of 150 minutes and 50 filter ratios around each CMP. Both SXT flux densities, measured with the Al.1 and AlMgMn filters, follow a steep rise during the AR emergence (July) and then a progressive decline with time. They have an evolution similar to the magnetic flux density (Fig. 3). The log-log plots of the flux densities versus $\bar{B}$ show that they follow a power law (Fig. 4) with very close exponents (1.87 ± 0.12 and 1.94 ± 0.12 for the full-resolution images).

We have also analyzed the half-resolution images, finding that their flux densities follow power laws with $\bar{B}$ with an exponent that depends slightly on the filter used but also on the duration of the exposures as follows: For short exposures we found exponents of 1.67 ± 0.27 and 1.82 ± 0.30 for the Al.1 and AlMgMn filters, respectively, while for long exposures these exponents are slightly lower: 1.51 ± 0.24 and 1.58 ± 0.27. The difference in the exponents between the two filters comes from their different sensitivity versus temperature. The difference in the exponents with the duration of the exposures is more surprising, since a routine analysis carries out exposure normalization. This is further analyzed in § 3.5.

3.5. *Sensitivity of the SXT Results to the Exposure Time*

Using the half-resolution images, we find that the fluxes deduced from the long exposures were lower than those deduced from the short exposures by a factor of ≈ 2 on July 10 and by a factor of ≤ 1.3 on August 2, while there were no differences later on (within the intrinsic variability of the AR). The exposure times also affect both the temperature (T) and the EM results. For temperature the exponents are 0.29 ± 0.12 and 0.14 ± 0.06 with short and long exposures, respectively, while for EM the exponents are 1.18 ± 0.33 and 1.05 ± 0.15, respectively. We found that when the AR was young and therefore very bright in SXT, observations taken with shorter exposure times gave higher T and EM results than the ones taken with longer exposures. This is surprising because we avoided all the flares above *GOES* class B and therefore a priori all the obvious saturated cases (see § 3.2). Our results could be interpreted as a small nonlinearity in the CCD response when the DN is high (e.g., Fernández Borda 2001). However, it is noteworthy that in half-resolution images, the DN values above the saturation level (DN = 255) are lost, while they are conserved in the full-resolution images (Tsuneta et al. 1991). This cannot be corrected by the software, and it can explain why exponents found using half-resolution images taken with long exposures are lower than those with short exposures. We did not find such a difference in the fluxes of the full-resolution images that are used in our analysis.

In the full-resolution images the observing sequence did not have image pairs with long and short exposures but instead combined (1) a thin Al filter image taken with a short exposure (typically 469 ms) with a Dagwood sandwich AlMgMn filter image taken with a long exposure (typically 2691 ms), and (2) the other dominant combination for image pairs, longer Al.1 filter exposures (typically 950 ms) and shorter AlMgMn filter exposures (typically 1357 ms). The combination of these two sets of image pairs slightly increased the scatter in the data; e.g., during the second rotation, image pair 1, on average, showed about 5% higher temperature and about 7% lower EM than pair 2. We emphasize again that this effect was still present after exposure normalization. However, since we saw no reason to prefer any exposure time combination, we used both image pairs 1 and 2 in the T and EM analyses presented. Finally, we note that the exponents obtained with the half-resolution images and short exposures are compatible, within the 3 σ error bars, with the exponents obtained with the full-resolution images. Because the latter are more reliable and have lower error bars, we use only the full-resolution images in the analysis described below.

4. EVOLUTION OF THE CORONAL TEMPERATURE

4.1. *SXT Temperature*

We used the filter ratio technique (Hara et al. 1992) and the GO_TEEM Solar Software (SSW) routine to compute

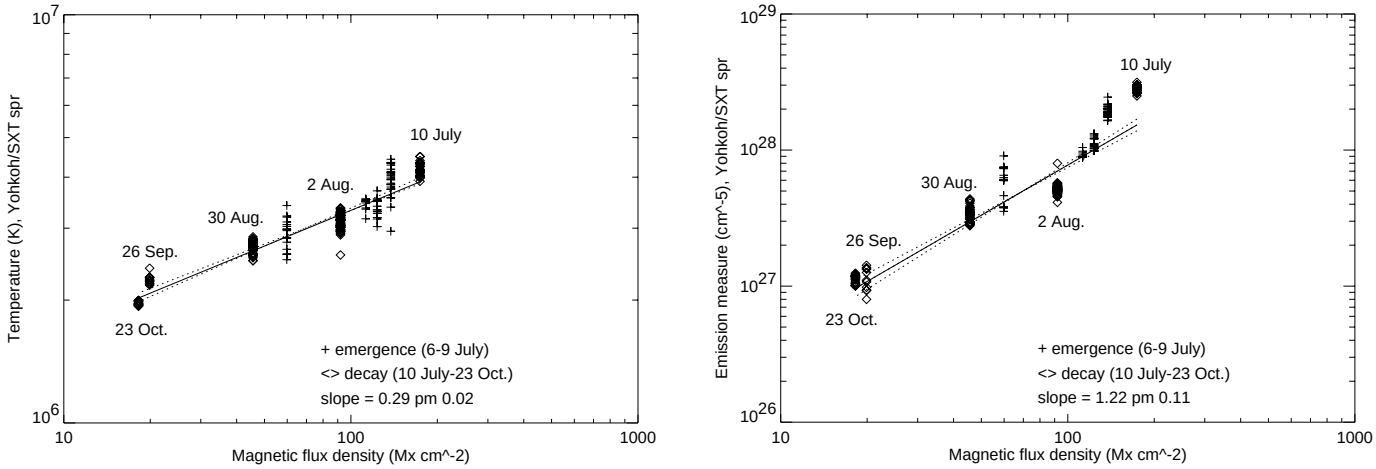

FIG. 5.—Plot of log-log curve of the temperature and EM derived from *Yohkoh*/SXT (full resolution) vs. magnetic flux density ($\bar{B}$). The convention for the marked points and least-squares fit is the same as in Fig. 4. The dispersion of the points for the same magnetic flux density reflects more the intrinsic variability of the AR than the random errors due to photon statistics (which are of the size of the plotted symbols).

the average coronal temperature of the AR, $\langle T \rangle_{\rm AR}$, from the mean flux densities observed in the AlMgMn and Al.1 filters (note that we use below the notation $\langle \ldots \rangle_{\rm AR}$ for all the volume averages in the corona, while we use a different notation for the photospheric average: $\bar{B}$). This average temperature is intensity weighted and likely to be biased toward hotter plasma, both because the temperature sensitivity of SXT favors hotter plasma and because hotter loops tend to be denser and therefore emit more strongly because of the N_e^2 dependence of the emissivity.

The temperature, when no significant brightenings were observed, shows a fast rise during the first vigorous flux emergence period, reaching 4.3 MK, followed by a gradual decay, reaching 2 MK by the fifth rotation in October (Fig. 3). The temperature changes in time in a way similar to the magnetic flux density, indicating a causal link between these two quantities. The log-log plot of $\langle T \rangle_{\rm AR}$ versus $\bar{B}$ shows that they are related through a power law (Fig. 5). The powers are very similar for the half-resolution and full-resolution data; however, the error bars are significantly lower in the full-resolution data; thus, the latter appear to be more reliable. The normal and the nonparametric statistics give very similar results for the derived powers: 0.29 ± 0.02 and $0.29^{+0.02}_{-0.02}$ for the full-resolution data.

4.2. *BCS Temperature*

BCS temperatures were estimated using the FIT_BCS spectral fitting routine within the SSW analysis system. The atomic data incorporated into the spectral fit are described in detail in Harra-Murnion et al. (1996). The software, written by D. Zarro and J. Lemen, uses a minimization χ^2 technique. The S XV channel includes the *w*, *x*, *y*, and *z* lines (notation by Gabriel 1972) with dielectronic satellites. The strong S XIV satellites *j* and *k* are almost coincident with the S XV forbidden line *z*. This blended feature has an intensity that decreases with T_e relative to the *w* line. The $n = 3$ satellites labeled d13 and d15, which are blended as a single feature to the long-wavelength side of the *w* line, have intensities that also decrease relative to the *w* line, as the temperature rises.

Typical spectra from each CMP studied are shown in Figure 6. The first spectrum shows a high temperature of 7.8 MK on July 8 that gradually declines to less than 2 MK on September 26. The change in the ratios of the lines can clearly be seen, in particular the decrease in the *w* line relative to the *z* line as the temperature decreases. It was not possible to fit the spectrum in September using the standard technique. The lowest temperature in our synthetic data is 2 MK. Sterling (1999) has studied in detail the September rotation, making a careful subtraction of the background flux. He showed that the temperature was roughly constant during the disk transit of the AR. Here, we use his mean value ($\langle T \rangle_{\rm AR} = 2.5$ MK) for this rotation.

The long-term change in BCS temperature is similar to the one shown by SXT temperature in Figure 3, but with higher values. The BCS temperature increases to between 6 and 7 MK during the first rotation and then decreases to ≥ 2 MK. Because of the higher initial temperature, the log-log plot of $\langle T \rangle_{\rm AR}$ versus $\bar{B}$ (Fig. 7) gives a steeper exponent for the BCS temperatures than for the SXT ones for both the normal and the nonparametric statistics: 0.35 ± 0.11 and $0.43^{+0.12}_{-0.14}$, respectively (see also Fig. 8). This suggests, as expected, that BCS observes a dominantly higher temperature plasma than SXT and that the highest temperatures tend to disappear faster when the magnetic flux density decreases.

5. EVOLUTION OF THE CORONAL EMISSION MEASURE

5.1. *SXT Emission Measure*

The SXT total EM was also computed using the filter ratio method. We derive a mean EM,

$$\langle \mathrm{EM} \rangle_{\rm AR} = \left\langle \int N_e^2 \, dl \right\rangle_{\rm AR}, \qquad (1)$$

by dividing the result by the area from which the emission came.

The $\langle \mathrm{EM} \rangle_{\rm AR}$ shows a sharp rise during the flux emergence and a more gradual decay during the ensuing rotations (Fig. 3). The log-log plots of $\langle \mathrm{EM} \rangle_{\rm AR}$ versus $\bar{B}$ indicate that these

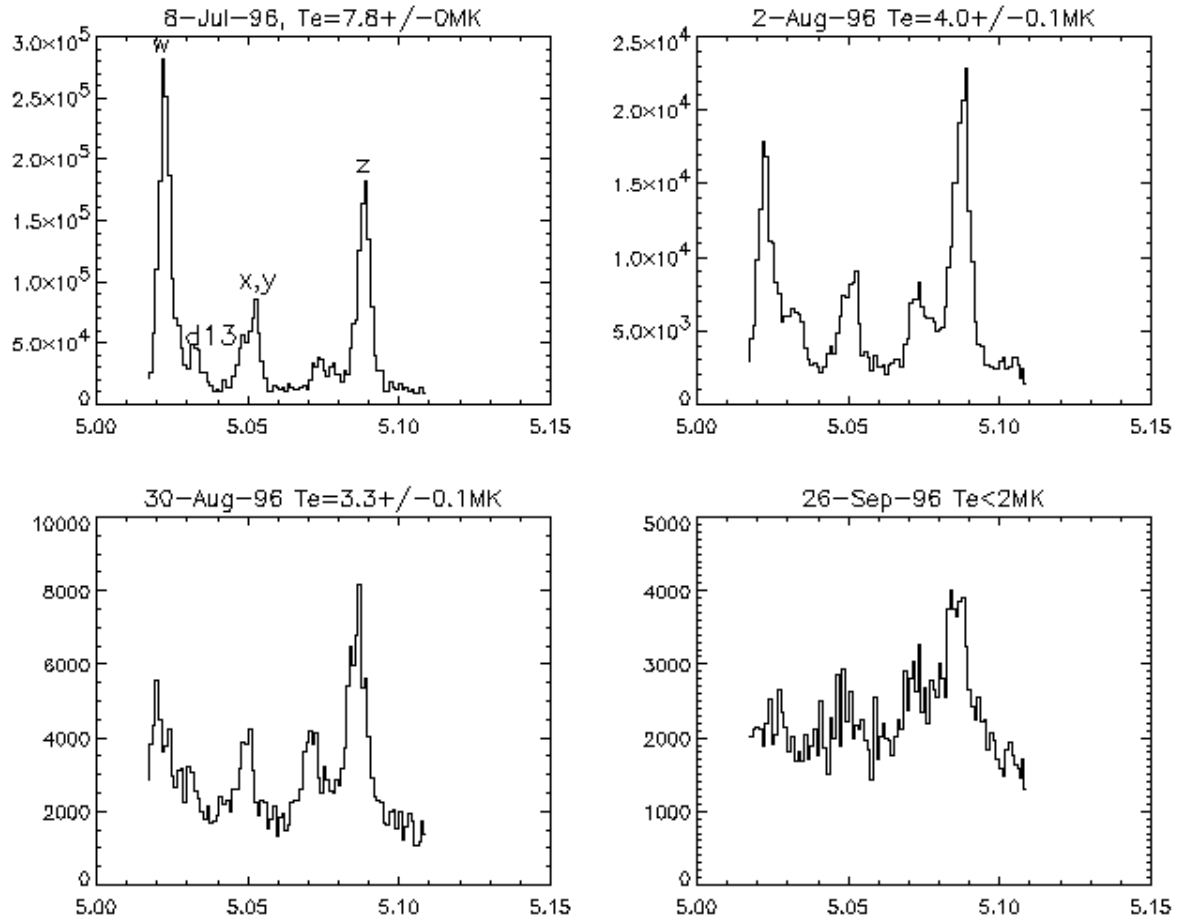

FIG. 6.—Example spectrum at each of the four CMPs studied. The temperatures of these individual spectra are listed above each plot. As the AR evolves, the emitted flux weakens and the spectra become noisier.

parameters are related following a power law (Fig. 5). Since we center our study in the decay phase of the AR life, the exponents listed in Table 1 represent only this period (July 10 to October 23). The nonparametric statistics give an exponent range that is shifted downward by 0.13 with respect to the result with the normal statistics. This is comparable to the estimated errors (see Fig. 8). Following Porter & Klimchuk (1995), we consider the nonparametric result to be more reliable.

5.2. *BCS Emission Measure*

Fits to the observed spectra of BCS also yield information on the EM. Since BCS is a full-disk instrument, we use the

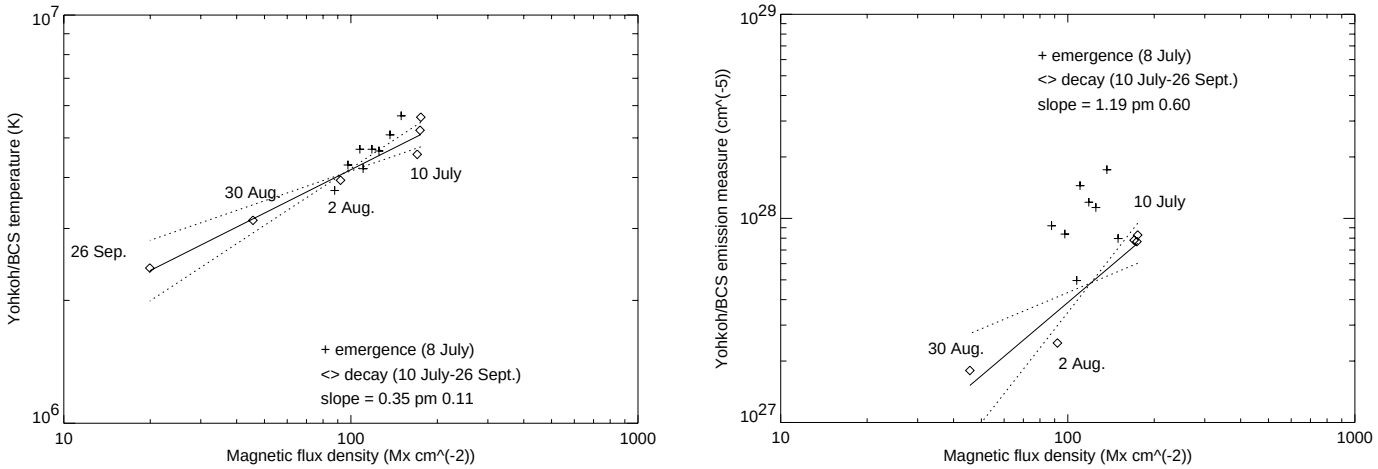

FIG. 7.—Plot of log-log curve of the temperature and EM derived from *Yohkoh*/BCS vs. magnetic flux density. The solid line shows the linear least-squares fit, and the two dotted lines correspond to the 3 σ error in the slope of the solid line. Only the decaying phase (*diamonds*) is included in the least-squares fit. The temperature and EM computed from BCS are higher and lower, respectively, than those from SXT (Fig. 5), while the slopes of the curves are comparable.

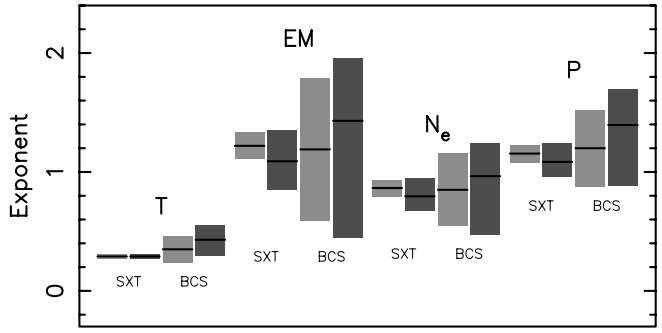

FIG. 8.—Ranges for the exponents found for the mean physical parameters in the scaling law equations: parameter $\propto \bar{B}^{\text{exponent}}$ ($\bar{B}$: magnetic flux density). The quantities T and EM are derived directly from the observations (§§ 4 and 5), and then N_e and P are deduced (§§ 6 and 7). The $\pm 3\ \sigma$ error range (99% confidence interval) for normally distributed statistics is light shaded. The confidence interval for nonparametric statistics is dark shaded (90% confidence interval for SXT; see § 3.3 for BCS).

same area as determined above with SXT to convert the global EM given by BCS to a mean EM (per unit surface area). We are supposing that most of the emission measured by BCS was coming from AR 7978. This is nearly true for SXT after the emergence phase (July 10) until October, since AR 7978 was alone on the Sun. The small and faint brightenings observed with SXT out of AR 7978 are expected to have an even smaller contribution in BCS data, because BCS is more sensitive to higher temperatures (see the comparison between the response functions of SXT and BCS in Fig. 4 of Sterling 1999). When AR 7978 was on the back side of the Sun, while no other AR was present on the disk, BCS spectra were very flat with no discernible lines (see Sterling 1999, Fig. 2*a*). When AR 7978 returned to the visible disk, BCS measured significant emitting spectral lines (Sterling 1999, Figs. 2*b* and 2*c*). Since this study was done for the September rotation, in which the BCS signal is the weakest of the ones analyzed here (see Fig. 6), and since AR 7978 was the only AR on the Sun during the analyzed period, we can safely assume that the emission detected by BCS was coming mostly from AR 7978.

The mean EM ($\langle \mathrm{EM} \rangle_{\mathrm{AR}}$) measured by BCS follows the trend of the mean SXT EM; the EM measured by BCS is approximately a factor of 2 lower than the EM measured by SXT (compare Fig. 5 with Fig. 7). The log-log plots of $\langle \mathrm{EM} \rangle_{\mathrm{AR}}$ versus $\bar{B}$ show a slope that is similar to the one of SXT. More precisely, the most probable value for the exponent is very close to the one of SXT, while the error bars are larger (Table 1).

6. SCALING LAWS FOR THE PLASMA DENSITY

The coronal plasma density is traditionally derived from the EM via the integral equation

$$\mathrm{EM} = \int N_e^2\, dl\ . \tag{2}$$

For coronal loops the integral path along the line of sight is usually taken as the observed transverse size of the loop (or a fraction of it if a filling factor is taken into account).

6.1. *Mean Plasma Density Derived from SXT*

In our case we have derived an averaged EM for the full AR (eq. [1]). The evolution of the photospheric field of AR 7978 is so simple (diffusion of a bipolar field) that we can reasonably assume a self-similar evolution of its magnetic configuration. That is to say, the magnetic configuration at a time t_1 is approximately the magnetic configuration at a time t_2 scaled spatially by the factor $(A_1/A_2)^{1/2}$, where A is the photospheric area of the AR as defined by MDI in § 3.1. With this hypothesis, the integral path in equation (1) scales as $\sqrt{A}$. This is supported by SXT limb observations that show that the vertical extent of AR emission tends to be proportional to the horizontal size of the region (e.g., Yashiro & Shibata 2001), and we further justify this for AR 7978 in the Appendix. Then, with $dl \propto \sqrt{A}$ and with the SXT results of Table 1, equation (1) gives

$$\langle N_e \rangle_{\mathrm{AR}} \propto \bar{B}^{0.87\pm0.07} \text{ for SXT},\quad \text{or } \bar{B}^{0.80^{+0.15}_{-0.13}}\ , \tag{3}$$

with the error bar coming from the intrinsic variability of the AR (outside flaring periods). The difference between the exponents found from the two statistics results mainly from the EM difference discussed in § 5. We note that, as for temperature, $\langle N_e \rangle$ is a weighted average. If N_e and T are

TABLE 1
EXPONENTS IN THE POWER-LAW FUNCTION

Parameter	Notation	Instrument	Gaussian Exponent	Nonparametric Exponent
Magnetic area	$\hat{A}$	MDI	-1.02 ± 0.18	$-1.00^{+0.15}_{-0.3}$
Mean temperature	$\hat{T}$	SXT	0.29 ± 0.02	$0.29^{+0.02}_{-0.02}$
Mean emission measure	$\widehat{\mathrm{EM}}$	SXT	1.22 ± 0.11	$1.09^{+0.26}_{-0.24}$
Mean density	$\hat{N}$	SXT	0.87 ± 0.07	$0.80^{+0.15}_{-0.13}$
Mean pressure	$\hat{P}$	SXT	1.15 ± 0.07	$1.09^{+0.15}_{-0.13}$
Mean temperature	$\hat{T}$	BCS	0.35 ± 0.11	$0.43^{+0.12}_{-0.14}$
Emission measure	$\widehat{\mathrm{EM}}$	BCS	1.19 ± 0.60	$1.43^{+0.53}_{-0.98}$
Mean density	$\hat{N}$	BCS	0.85 ± 0.30	$0.96^{+0.28}_{-0.49}$
Mean pressure	$\hat{P}$	BCS	1.20 ± 0.32	$1.39^{+0.30}_{-0.51}$

NOTES.—Exponents b in the power-law function $a\bar{B}^b$ are fitted to MDI magnetic area, SXT full-resolution data, and BCS data, temperature, and EM as functions of the magnetic flux density ($\bar{B}$) in AR 7978. The period of time is limited to July 10 to October 23 (September 26 for BCS) to study the quiet phase. The exponent b of a given physical quantity is noted with a hat on top of the quantity notation. The results with normally distributed (Gaussian) statistics and with nonparametric statistics are given with a $\pm 3\ \sigma$ error range (99% confidence interval) and with a 90% confidence interval as $\pm$ (see § 3.3 for BCS).

positively correlated, as expected, then the temperature response of SXT favors denser plasma. Furthermore, there is an additional density weighting due to the fact that the intensity scales as N_e^2 and that $(\langle N_e^2 \rangle)^{1/2}$ is larger than $\langle N_e \rangle$.

6.2. *Mean Plasma Density Derived from BCS*

In the case of BCS, we have no information on the spatial location of the emitting material. Since the EM shows the same trend for both BCS and SXT (§ 5), we make the same hypothesis for the integral path along the line of sight as above: $dl \propto \sqrt{A}$. We then obtain a scaling law for density versus $\bar{B}$ that is similar to that obtained from SXT data, but with a larger error bar:

$$\langle N_e \rangle_{\rm AR} \propto \bar{B}^{0.85\pm0.30} \text{ for BCS},$$
$$\text{or } \bar{B}^{0.96^{+0.28}_{-0.49}}. \quad (4)$$

7. SCALING LAWS FOR THE PLASMA PRESSURE

In the present section we use the scaling laws (temperature and EM vs. magnetic flux density) obtained from observations (§§ 4 and 5) to deduce the scaling laws for the coronal pressure.

7.1. *Plasma Pressure Derived from SXT*

Using the average temperature (§ 4) and the average density determined by the EM (assuming $dl \propto \sqrt{A}$), we have the following scaling for the average plasma pressure:

$$\langle P \rangle_{\rm AR} \propto \bar{B}^{1.15\pm0.07} \text{ for SXT},$$
$$\text{or } \bar{B}^{1.09^{+0.15}_{-0.13}}. \quad (5)$$

Here, we have implicitly assumed that the product of the two averaged quantities (density and temperature) gives the average pressure. The error is computed assuming that the density and temperature errors are statistically independent.

Although not entirely independent, there is another way to obtain the average plasma pressure from SXT called the "single-filter method" (e.g., see Hara 1996). The plasma pressure can be expressed directly as a function of DN (a direct measure of the energy received by the detector) as follows:

$$\langle P \rangle_{\rm AR} = 2k_{\rm B} \sqrt{\frac{T^2}{f(T)}} \sqrt{\frac{\rm DN}{\delta t\, l}}, \quad (6)$$

where $k_{\rm B}$ is the Boltzmann constant, $f(T)$ is the SXT response function, δt is the exposure duration, and l is the length along the line of sight of the emitting plasma. The function $D(T) = [T^2/f(T)]^{1/2}$ depends only weakly on the temperature in the range 2×10^6 K $< T < 5 \times 10^6$ K for both the Al.1 and AlMgMn filters used here (see Fig. 2.5 of Hara 1996). Then, we simply have

$$\langle P \rangle_{\rm AR} \propto \sqrt{\frac{\rm DN}{\delta t\, l}}. \quad (7)$$

Applying this to the data for both filters (Fig. 4), we find

$$\langle P \rangle_{\rm AR} \propto \bar{B}^{1.19\pm0.07} \text{ for Al.1}, \quad (8)$$
$$\langle P \rangle_{\rm AR} \propto \bar{B}^{1.23\pm0.07} \text{ for AlMgMn}. \quad (9)$$

This is fully compatible with the result of equation (5), providing an internal test of the SXT results.

7.2. *Plasma Pressure Derived from BCS*

Using the average temperature (§ 4) and the average density determined by the EM (assuming $dl \propto \sqrt{A}$), we have the following scaling for the average plasma pressure:

$$\langle P \rangle_{\rm AR} \propto \bar{B}^{1.20\pm0.32} \text{ for BCS},$$
$$\text{or } \bar{B}^{1.39^{+0.30}_{-0.51}}, \quad (10)$$

a law that is consistent, within the error bars, with the one found with SXT (eq. [5]).

7.3. *Comparison with other Estimations*

The four equations (5) and (8)–(10) give exponents lower than the result found by Golub et al. (1980). These authors determined that $\langle P \rangle_{\rm AR} \propto \bar{B}^{1.6}$, with an exponent in the range [1.5, 1.9]. However, the slope of the function plotted in their Figure 2*b* is ≈1.3. Redoing a standard least-squares fit from their data, Yashiro & Shibata (2001) found $P \propto \bar{B}^{1.11\pm0.64}$, while Sturrock & Uchida (1981) noted previously that after removing one data point to have a coherent set of data, the fit was $P \propto \bar{B}^{0.8\pm0.6}$ (this point came from another kind of study). We confirm these two latter results. We conclude that our result is indeed fully compatible with Golub et al., although with their data, not with their published exponent.

We now compare our results with the results of Porter & Klimchuk (1995) for SXT loops ($P \propto L^{-0.96^{+0.74}_{-0.86}}$) and Mandrini et al. (2000a) for the decrease of the magnetic field with loop length ($\langle B \rangle_{\rm loop} \propto L^{-0.88\pm0.3}$) and obtain $P \propto \langle B \rangle_{\rm loop}^{1.09\pm0.8}$. This is compatible with equations (5) and (8)–(10).

The largest difference was found when comparing our results with Yashiro & Shibata (2001), who obtained $P \propto \bar{B}^{0.78\pm0.23}$ from the analysis of 31 ARs at selected times. This inconsistency within the 3 σ error bars is surprising, since they have also used MDI and SXT (even the same filters), as well as the assumption that $dl \propto \sqrt{A}$, and a comparable range of magnetic flux density, and they have analyzed the ARs globally. The main difference between the two studies is that they took snapshots of 31 young ARs, while we are studying the long-term evolution of a single AR. Yashiro & Shibata (2001) analyzed mainly small and medium-sized ARs with sizes less than 150 Mm. In addition, only four of their largest ARs had similar total magnetic flux to AR 7978, studied by us. The assumption that $dl \propto \sqrt{A}$ is valid for loops that are lower than the pressure scale height. In our case a small fraction of the faint loops have heights larger than the pressure scale height in the later phase of the AR's lifetime. Hence, if we use the hypothesis $dl \propto s_P$ instead, we get $\langle P \rangle_{\rm AR} \propto \bar{B}^{0.75\pm0.06}$ and $\propto \bar{B}^{0.69^{+0.13}_{-0.12}}$ for the two statistics, respectively, a result that is in close agreement with Yashiro & Shibata (2001). Nevertheless, we show in the Appendix that the EM decreases exponentially with height, with a vertical scale defined by the horizontal extension of the AR ($\sqrt{A}$) and not by the pressure scale height (s_P). Then, the origin of the difference with the results of Yashiro & Shibata (2001) remains unexplained.

We have analyzed the decay phase of AR 7978. As an AR decays, its properties are expected to become closer to those of quiet regions (with an enhanced network), and hence we compare our results with those of Hara (1998). He found that the soft X-ray flux of the quiet Sun scales as $\Phi^{3.3\pm0.3}$,

where Φ is the total quiet-Sun magnetic flux. Using equation (6) for the quiet Sun, we get $\langle P \rangle_{QS} \propto \bar{B}^{1.65\pm0.15}$. Therefore, our result for a decaying region is in between the one for young ARs and the one for quiet regions. However, it is worth mentioning that Pevtsov & Acton (2001) found little correlation between the X-ray emission above quiet regions and the corresponding underlying magnetic field. They concluded that this emission could be the result of the large-scale magnetic relaxation of the magnetic field coming from ARs. Another contribution comes from the streamers associated with ARs that appear in projection over quiet regions (Li et al. 2002). Then, the link between X-ray flux and underlying magnetic field found by Hara (1998) is likely to have a less direct interpretation than in situ coronal heating. A recent work by Benevolenskaya et al. (2002) showed that the average *Yohkoh* soft X-ray intensity of the corona is proportional to B^a, with B being the mean unsigned longitudinal flux from the Kitt Peak Observatory synoptic maps. They found that the exponent a has a solar cycle variation: the exponent a appears to be higher during the declining phase and minimum (2–2.2) than during the rising phase and maximum (1.6–1.8) of the solar cycle. Note that our analysis has been carried out during a solar activity minimum.

8. CONCLUSION

An isolated active region (AR 7978) was well observed on the Sun during five solar rotations, starting in 1996 July. This fact provides a unique opportunity to analyze the long-term evolution of the coronal plasma parameters as the magnetic configuration expands in size. Because AR 7978 was nearly alone on the Sun, a large set of *Yohkoh* data with different spatial and temporal resolutions is available. Using these data, together with MDI longitudinal magnetograms, we are able to study how the variation of the plasma physical parameters correlates with the magnetic field evolution. Analyzing the temporal variation of the fluxes measured with *GOES* and SXT (see § 3.2), we select observing periods outside any significant brightening enhancement to obtain information about the evolution of the quasi-static corona.

We find that the SXT fluxes (Al.1 and AlMgMn filters), as well as the mean temperature and EM derived from SXT and BCS, are well described by power laws ($\propto \bar{B}^b$) of the average magnetic flux density $\bar{B}$ (total unsigned magnetic flux divided by the photospheric area of the AR) as shown in Figures 4, 5, and 7. The underestimation of the strong magnetic fields with MDI (§ 3.1) has only a minor effect on our power laws, which are mainly defined by the decay phase of the AR, when the magnetic flux densities are low enough that MDI response is in the linear regime. The exponents (b) of these power-law functions ($a\bar{B}^b$) are derived using two different statistical methods: a classical least-squares method in log-log plots and a nonparametric method, which takes into account the fact that errors in the data may not be normally distributed. The exponents found are summarized in Figure 8 and Table 1 for the temperature and the EM, together with those of the derived density and pressure. We obtain compatible results for SXT and BCS, within the error bars. The error bars given by both statistical methods are similar (with a 99% and 90% confidence interval, respectively). We conclude that the coronal plasma temperature and EM, as well as all derived quantities (such as density and pressure), have a power-law dependence on $\bar{B}$.

As discussed in § 1, a primary motivation for determining these scaling-law relationships is to test the various theoretical ideas of coronal heating that have been proposed. The details of how we accomplish this is presented in a companion paper (Démoulin et al. 2003). Briefly, we combine our observational scaling laws with quasi-static equilibrium loop theory to obtain a new scaling law involving the volumetric heating rate and the average magnetic flux density. The power-law exponent of this new scaling law is then compared with the exponents predicted by the various coronal heating models. Since different models predict different exponents, this serves as a powerful way of discriminating among them. The basic strategy is similar to the one we have used previously to test coronal heating models with observations of individual coronal loops (Mandrini et al. 2000a). It is quantitative studies such as these that offer the best hope of solving the fundamental question of what makes the corona so hot.

We thank the referee, K. Shibata, for constructive comments on the paper. The authors thank the *SOHO*/MDI consortium for the *SOHO* data and the Mullard Space Science Laboratory (MSSL) Solar UK Research Facility (SURF) for *Yohkoh* data. *SOHO* is a joint project by ESA and NASA. P. D. and C. H. M. acknowledge financial support from ECOS (France) and SECyT (Argentina) through their cooperative science program (A01U04). L. v. D.-G. was supported by Hungarian government grants OTKA T-038013 and T-032846 and by research fellowship F/01/004 of the Katholieke Universiteit Leuven. P. D. and L. v. D.-G. acknowledge the Hungarian-French Science and Technology cooperative program. C. H. M. is grateful for an MSSL, University College London (UCL), visitor's grant. The work of J. A. K. was supported by NASA and the Office of Naval Research. P. D., L. v. D.-G., and L. K. H. acknowledge travel support from the Royal Society Joint Project (MSSL/UCL–Observatoire de Paris, Meudon) and PPARC for the award of an advanced fellowship. We thank Loren Acton and Roberto Fernández Borda for helpful discussions. We thank L. M. Green for discussions and measurements on MDI calibration.

APPENDIX

EMISSION MEASURE SCALE HEIGHT

In § 6.1 we assume that the vertical extension of the plasma is proportional to the AR horizontal size. More precisely, we use

$$\int N_e^2 \, dl \propto \langle N_e \rangle_{AR}^2 \sqrt{A} \, , \tag{A1}$$

where A is the photospheric area of the AR as defined by MDI in § 3.1. The above hypothesis that $dl \propto \sqrt{A}$ does not hold for

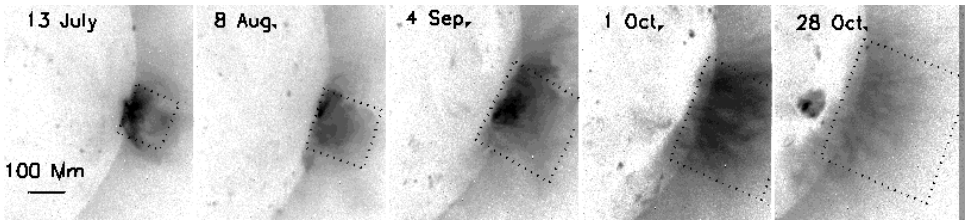

FIG. 9.—Evolution of the AR SXT emission (DN) at the west limb. The dotted square shows the photospheric surface of the AR estimated at the time of the observation.

loops that have a top height of the order of or higher than the pressure scale height (s_P). As the mean temperature decreases with time from $\approx 4 \times 10^6$ K on July 10 to $\approx 2 \times 10^6$ K on October 23 (see Fig. 3), s_P decreases from $\approx$200 to $\approx$100 Mm, while the AR and the loops increase in size (see Figs. 1 and 2; $\sqrt{A} \approx 300$ Mm on October 23). The pressure scale height limitation on *dl* then becomes more important with time. We justify the use of equation (A1) using three independent arguments as follows.

First, the height of the SXT loops can be estimated using a magnetic extrapolation of the MDI magnetograms (adjusting the magnetic shear to best fit the SXT loops; see van Driel-Gesztelyi et al. 1999a; Mandrini et al. 2000b; Démoulin et al. 2002). We have found that a number of faint loops from the end of August to October have a height comparable to s_P. It is difficult to follow these faint loops along their length and to say whether they were depleted from plasma at their top or not, but the magnetic extrapolations show that the brightest SXT loops have a top height below s_P from July to October. We conclude that the global EM of the AR should mostly be affected by these bright loops, so that we can use equation (A1).

Second, since the gravitational limitation imposed on the plasma height is expected to increase with time (s_P is decreasing while $\sqrt{A}$ is increasing), its effect, if any, should be most pronounced at later times. The EM decreases with time as the magnetic field becomes weaker (Fig. 5). Gravitational stratification is certainly not the cause of this decrease in the early rotations, when $s_P > \sqrt{A}$. If it were important in the later rotations, it would be manifested as an additional decrease in the EM, beyond the trend that is present in the early rotations. There is no evidence for such an accelerated decrease. The scaling law exponent $\widehat{\mathrm{EM}}$ is essentially unaffected when we exclude either the last or the last two rotations from the analysis: $\widehat{\mathrm{EM}} = 1.09^{+0.26}_{-0.24}$ for the full period of July 10 to October 23, $\widehat{\mathrm{EM}} = 1.17^{+0.22}_{-0.36}$ for the reduced period of July 10 to September 26, and $\widehat{\mathrm{EM}} = 1.03^{+0.58}_{-0.31}$ for the further reduced period of July 10 to August 30.

Finally, we analyze the flux and the EM dependence with height when the AR was at the west limb (to have the closest temporal measurements from CMP for all rotations). Figure 9 shows that the X-ray emission extends both horizontally and vertically as $\approx\sqrt{A}$ (this is confirmed by analyzing vertical cuts as we show below for the EM). Because the height dependence of the EM is more crucial for our analysis (§ 6.1), we describe it in more detail below. The logarithm plot of the EM versus height (Fig. 10) is almost linear for all rotations, except at the larger heights where the signal is still too noisy even with the averaging done (we have averaged five EM profiles measured in nine EM maps for all the rotations; thus, the profiles represent 45 measurements each). It shows that the EM has an exponential decrease with height. Its scale height L_{EM} (defined by an *e*-folding factor) is nearly proportional to $\sqrt{A}$ (Fig. 11), further justifying the use of equation (A1). A least-squares fit gives

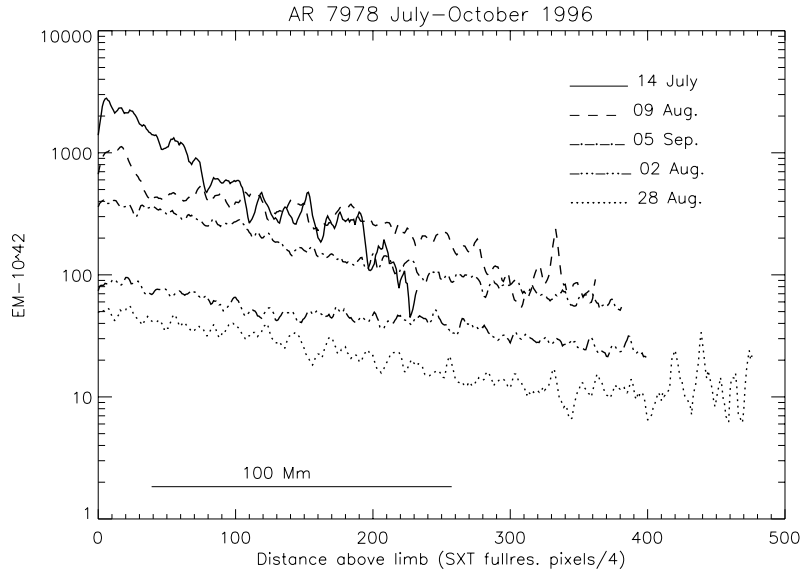

FIG. 10.—Evolution of log EM derived from *Yohkoh*/SXT (full resolution) vs. height above the west limb after the CMP of the studied rotations. Each EM plotted is an average of approximately 45 cuts (nine close times without significant activity with five cuts scanning the AR; the saturated region, when present, has been avoided).

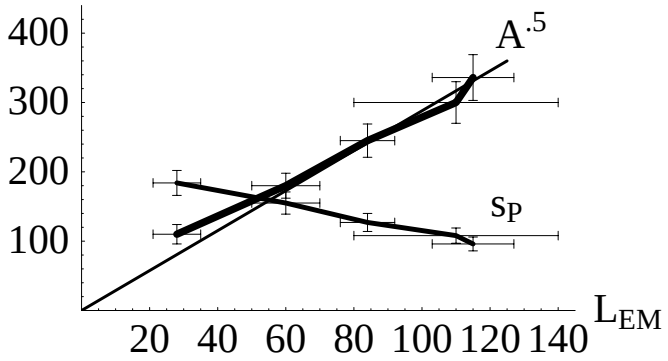

FIG. 11.—Evolution of the AR horizontal extension $\sqrt{A}$ (where A is the photospheric area of the AR as defined by MDI in § 3.1) and of the pressure scale height (s_P) with respect to the EM scale height ($L_{\rm EM}$, defined by an e-folding factor). The units are in Mm. The straight line shows the linear least-squares fit: $\sqrt{A} = 2.9L_{\rm EM}$. The quantity $L_{\rm EM}$ is approximately proportional to $\sqrt{A}$, while it varies inversely with s_P, indicating that the vertical extent of the plasma distribution is controlled by the magnetic field (and coronal heating) rather than by gravitational stratification.

$L_{\rm EM} = 0.35\sqrt{A}$ so that the vertical extension is proportional to, but lower than, the horizontal extension of the AR. However, the pressure scale height s_P decreases with $L_{\rm EM}$ and becomes comparable to it only during the last two rotations. The average plasma density has a scale height measured at the limb that is not determined by s_P but rather by the photospheric extension of the AR (density scale height $\approx 2L_{\rm EM} \approx 0.7\sqrt{A}$) . The distribution of the plasma in the AR is then dominantly determined by the magnetic field, via the heating distribution, rather than the gravitational stratification.

REFERENCES

Arndt, M. B., Habbal, S. R., & Karovska, M. 1994, Sol. Phys., 150, 165
Aschwanden, M. J., et al. 2000, ApJ, 531, 1129
Benevolenskaya, E. E., Kosovichev, A. G., Lemen, J. R., Scherrer, P. H., & Slater, G. L. 2002, ApJ, 571, L181
Berger, T. E., & Lites, B. W. 2002, Sol. Phys., submitted
Brosius, J. W., Davila, J. M., Thomas, R. J., Saba, J. L. R., Hara, H., & Monsignori-Fossi, B. C. 1997, ApJ, 477, 969
Culhane, J. L., et al. 1991, Sol. Phys., 136, 89
Delaboudinière, J. P., et al. 1995, Sol. Phys., 162, 291
Démoulin, P., van Driel-Gesztelyi, L., Mandrini, C. H., Klimchuk, J. A., & Harra, L. 2003, ApJ, 586, 592
Démoulin, P., et al. 2002, A&A, 382, 650
Dere, K. P., Landi, E., Young, P. R., & Del Zanna, G. 2001, ApJS, 134, 331
Fernández Borda, R. 2001, Ph.D. thesis, Univ. Buenos Aires
Gabriel, A. H. 1972, Space Sci. Rev., 13, 655
Gerassimenko, M., & Nolte, J. T. 1978, Sol. Phys., 60, 299
Golub, L., & Herant, M. 1989, Proc. SPIE, 1160, 629
Golub, L., Maxson, C., Rosner, R., Serio, S., & Vaiana, G. S. 1980, ApJ, 238, 343
Handy, B. N., et al. 1999, Sol. Phys., 187, 229
Hara, H. 1996, Ph.D. thesis, Univ. Tokyo
———. 1998, in Observational Plasma Astrophysics: Five Years of *Yohkoh* and Beyond, ed. T. Watanabe, T. Kosugi, & A. C. Sterling (Astrophys. & Space Sci. Library 229; Dordrecht: Kluwer), 3
Hara, H., Tsuneta, S., Lemen, J. R., Acton, L. W., & McTierman, J. M. 1992, PASJ, 44, L135
Harra-Murnion, L. K., et al. 1996, A&A, 308, 670
Kano, R., & Tsuneta, S. 1995, ApJ, 454, 934
———. 1996, PASJ, 48, 535
Klimchuk, J. A., & Gary, D. E. 1995, ApJ, 448, 925
Li, J., LaBonte, B., Acton, L., & Slater, G. 2002, ApJ, 565, 1289
Liu, Y., & Norton, A. A. 2001, SOI Technical Note SOI-TN-01-144 (Stanford: SOI)
Mandrini, C. H., Démoulin, P., & Klimchuk, J. A. 2000a, ApJ, 530, 999
Mandrini, C. H., van Driel-Gesztelyi, L., Thompson, B., Plunkett, S., Démoulin, P., & Aulanier, G. 2000b, Int. Geophys., 39(1), 73
Orlando, S., Khan, J., van Driel-Gesztelyi, L., Thompson, B., Fludra, A., & Foing, B. 2000, Adv. Space Res., 25, 1913
Pevtsov, A. A., & Acton, L. W. 2001, ApJ, 554, 416
Porter, L. J., & Klimchuk, J. A. 1995, ApJ, 454, 499
Rosner, R., Tucker, W. H., & Vaiana, G. S. 1978, ApJ, 220, 643
Scherrer, P. H., et al. 1995, Sol. Phys., 162, 129
Serio, S., Peres, G., Vaiana, G. S., Golub, L., & Rosner, R. 1981, ApJ, 243, 288
Shimojo, M., Hara, H., & Kano, R. 2002, in COSPAR Colloq. 13, Multi-Wavelength Observations of Coronal Structure and Dynamics: *Yohkoh* 10th Anniversary Meeting, ed. P. C. H. Martens & D. P. Cauffman (Boston: Pergamon), 419
Sterling, A. C. 1999, A&A, 346, 995
Sturrock, P. A., & Uchida, Y. 1981, ApJ, 246, 331
Tsuneta, S., et al. 1991, Sol. Phys., 136, 37
Underwood, J. H., & McKenzie, D. L. 1977, Sol. Phys., 53, 417
Vaiana, G. S., Krieger, A. S., & Timothy, A. F. 1973, Sol. Phys., 32, 81
Vaiana, G. S., Van Speybroeck, L., Zombeck, M. V., Krieger, A. S., Silk, J. K., & Timothy, A. F. 1977, Space Sci. Instrum., 3, 19
van Driel-Gesztelyi, L. 1998, in ASP Conf. Ser. 155, Three-Dimensional Structure of Solar Active Regions, ed. C. Alissandrakis & B. Schmieder (San Francisco: ASP), 202
van Driel-Gesztelyi, L., et al. 1999a, in ASP Conf. Ser. 184, Magnetic Fields and Oscillations, ed. B. Schmieder, A. Hofmann, & J. Staude (San Francisco: ASP), 302
———. 1999b, in Proc. 8th *SOHO* Workshop on Plasma Dynamics and Diagnostics in Transition Region and Corona, ed. B. Kaldeich-Schürmann (ESA SP-446; Noordwijk: ESA), 663
Watanabe, T., et al. 1995, Sol. Phys., 157, 169
Yashiro, S., & Shibata, K. 2001, ApJ, 550, L113
Yoshida, T., Tsuneta, S., Golub, L., Strong, K., & Ogawara, Y. 1995, PASJ, 47, L15